A hybrid Machine Learning unmixing method for automatic analysis of γ-spectra with spectral variability

Dinh Triem Phan[a,*], Jérôme Bobin[b], Cheick Thiam[a], Christophe Bobin[a]

[a] *Université Paris-Saclay, CEA, List, Laboratoire national Henri Becquerel (LNE-LNHB), Palaiseau, 91120, France*
[b] *IRFU, CEA, Universite Paris-Saclay, Gif-sur-Yvette, 91191, France*

Abstract

Automatic identification and quantification of γ-emitting radionuclides, taking into account spectral deformations due to γ-interactions in radioactive source surroundings, is a challenging task in the nuclear field. In that context, this paper presents a Machine Learning approach based on autoencoder that can learn a model for the spectral signatures of γ-emitters with variability. Training and test datasets were obtained by means of simulated γ-spectra computed with the Geant4 simulation code according to increasing material thicknesses (steel, lead). A novel hybrid unmixing algorithm combining a pretrained autoencoder is studied for joint estimation of spectral signatures and counting in the case of mixtures of four radionuclides (^{57}Co, ^{60}Co, ^{133}Ba, ^{137}Cs). The investigations were carried out to account for spectral deformations due to attenuation, Compton scattering and fluorescence at high and low statistics. This study demonstrates the validity of this novel hybrid approach combining Machine Learning and Maximum Likelihood for the automatic full-spectrum analysis of γ-spectra.

Keywords: Gamma-ray spectrometry, Spectral variability, Hybrid algorithm, Machine Learning, Interpolating autoencoder, Semi-blind unmixing

1. Introduction

Gamma-ray spectrometry is a classical technique allowing the identification and quantification of γ-emitting radionuclides in many fields of nuclear applications. In radioactivity laboratories, experimental γ-spectra are traditionally analyzed by experts by considering the full-absorption peaks corresponding to the γ-photon energies related to radionuclide decay schemes. The classical procedure is based on peak-fitting techniques assuming that counting follows Gaussian statistics. Alternative approaches are required for automatic analysis of γ-spectra with robust decision-making for non-expert users or to help experts

*Corresponding author
Email address: dinh-triem.phan@cea.fr (Dinh Triem Phan)

in the case of complex mixtures of γ-emitters. The need for specific algorithms is essential for various applications such as fast spectroscopic identification for environmental measurements (e.g., following a radiological or nuclear accident), decommissioning of nuclear facilities or security screening. In the literature, the general trend is to address these issues by implementing Machine Learning (ML) algorithms [1]. For instance, the problem of identifying γ-emitters can be considered binary or multi-class multi-label classification in ML. Several architectures are proposed in the literature, such as Multilayer Perceptron (MLP) [2], Convolutional Neural Network (CNN) [3] or Recurrent Neural Network (RNN) [4]. Additional techniques can be used to improve the accuracy and to guarantee the robustness of the neural network, such as adversarial learning [5] or CNN/RNN to learn new features in combination with MLP [4]. In general, the interpretability of ML developments for γ-spectrometry is limited compared to classical statistical techniques (decision-making, uncertainty assessment). For instance, full-spectrum analysis based on Poisson statistics yields good performances for fast identification and quantification of γ-emitting radionuclides at low statistics. This approach can be addressed through the Maximum Likelihood Estimation (MLE) based on the application of spectral unmixing [6][7]. This technique aims at decomposing an experimental γ-spectrum into individual spectral signatures corresponding to the detector response for the γ-photon emission of the radionuclides to be identified. The combination with sparsity applied for selecting the minimum number of spectral signatures that explain a measured γ-spectrum leads to robust identification and quantification in the case of complex mixtures of γ-emitters [6][7].

Spectral unmixing has been validated using fixed spectral signatures corresponding to well-defined measurement conditions [6][7]. However, the shape variability of experimental γ-spectra can be induced by Compton scattering, attenuation or fluorescence phenomena due to photon interactions surrounding radioactive sources. Although the attenuation problem is addressed in a few articles ([8] and [9]), the current state-of-the-art of spectral unmixing methods is not well suited to consider accurately the variability of the spectral signatures, the mixture model and the Poisson statistics. Accounting for these issues is key to providing an accurate and low-bias unmixing procedure, especially in the low statistics limits. To that end, this paper presents a novel hybrid unmixing method that combines a standard statistical approach based on MLE and a ML-based model of the radionuclide spectral signatures to capture their variability. Since no analytical model is available to describe spectral deformations, Interpolating AutoEncoder (IAE) is implemented to learn radionuclide spectral signatures with variability using simulated spectra obtained with the Geant4 simulation code [10].

The article is organized as follows:

- Section 2 presents the Geant4-based Monte Carlo (MC) simulations implemented to obtain the γ-spectra dataset with spectral deformations for various radionuclides (^{57}Co, ^{60}Co, ^{133}Ba, ^{137}Cs) due to physical effects

such as attenuation, Compton scattering and fluorescence. For the validation of the hybrid ML approach, a simple geometry based on a point source in a steel or lead sphere with increasing thicknesses (up to 30 mm) and a 3"Œ3" NaI(Tl) scintillation detector was constructed.

- The description of the IAE model is given in Section 3. Two approaches to modeling the γ-spectrum deformations are proposed: an individual model that learns for each radionuclide independently and a joint model for all radionuclides that captures the correlations between the radionuclide spectral variability. The reconstruction performance of the IAE model is then assessed.

- In Section 4, a novel semi-blind full-spectrum unmixing algorithm for joint estimation of radionuclide spectral signatures and their mixing weights is introduced. For that purpose, a Block Coordinate Descent (BCD) minimization scheme is implemented using the IAE model as a constraint on spectral signatures. The hybrid ML approach is assessed in 5 using mixtures of simulated spectra of the four radionuclides with an experimental natural background at high and low statistics.

2. Geant4 simulations of spectral signature deformations

2.1. Simulations of attenuation and Compton scattering effects in a steel sphere

A γ-ray spectrum is mainly featured by full-absorption peaks, pair production and Compton continuum depending on the γ-photon energies emitted by the radionuclides present in a radioactive source. The overall shape is sensitive to experimental conditions due to γ-photon interactions in the surrounding materials and the detector. The resulting effect may be significant variations in the peak-to-Compton ratios. For the validation of the hybrid ML approach, the datasets representing the γ-spectra deformations were obtained by means of MC simulations of radiation-matter interactions in a 3"Œ3" NaI(Tl) scintillation detector using Geant4 - a general MC tool for the simulation of passage of particles through the matter [10]. The γ-emission was considered for four radionuclides covering a large range of energies between 20 keV and 1600 keV: ^{57}Co, ^{60}Co, ^{133}Ba, ^{137}Cs. These radionuclides are classical γ-emitters available in standards addressing handheld instruments or spectroscopy-based portal monitors (e.g., ANSI N42.38-2015 [11]). Regarding the Geant4 simulations, the 3"Œ3" NaI(Tl) detector is modeled by considering the scintillation crystal's geometry and housing, which has a total thickness of 2 mm. The reflector has a thickness of 1.5 mm of alumina, while the remaining 0.5 mm is composed of aluminum. Regarding the radioactive source, a simple geometry was considered involving the γ-rays emission from a point source located in a steel sphere positioned 20 cm from the front of the detector.

The choice of source shielding made of steel was taken from the standards mentioned above. For each radionuclide, different spectral signatures were obtained with Geant4 simulations with increasing sphere thickness ranging from

0.001 mm to 30 mm. Because low-energy photons (lower than 100 keV) are sensitive to attenuation, 25 thickness steps were chosen between 0.001 mm and 2 mm of steel. For larger thicknesses up to 30 mm corresponding to an increase of Compton scattering, a constant step equal to 0.4 mm was adopted. Fig. 1 displays the evolution of the simulated spectral signatures of ^{60}Co and ^{133}Ba as a function of steel thickness. The total number of spectral signatures for each radionuclide is equal to 96. For each simulated spectral signature, the emitted γ-photons follow the specific decay scheme for each radionuclide and the total number of emitted γ-rays is around 250 million. The energy resolution of the NaI(Tl) detector was taken into account (6.5 keV at 662 keV). Each spectral signature is featured by 800 channels with a binning of 2 keV per channel and a low-energy cut-off equal to 18 keV to consider the 32-keV X-ray emission of ^{137}Cs.

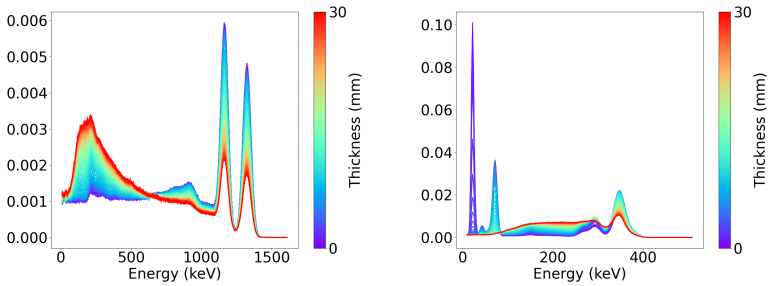

Fig. 1. Evolution of the simulated spectral signatures of ^{60}Co (left) and ^{133}Ba (right) as a function of steel thickness. The y-axis represents normalized amplitudes. The blue curves correspond to low thicknesses and the red curves correspond to high thicknesses.

2.2. Simulations of fluorescence, attenuation and Compton scattering effects in a lead sphere

In order to extend the validation of the hybrid ML approach to the fluorescence effect, spectral signatures were simulated for the same radionuclides in the case of a lead sphere. Fluorescence corresponds to the emission of secondary X-ray photons following photoelectric absorption of primary γ-photons. The atomic rearrangement occurring subsequently to an electron ejection can yield X-ray emission with energies depending on the materials in which the γ-rays interaction occurs. As shown in Fig. 2 in the case of simulations with a lead sphere, a new peak appears in the spectral signatures for ^{57}Co and ^{137}Cs corresponding to X_K photons having energies between 70 keV and 90 keV. As explained for the simulations with the steel sphere and due to the greater density of lead, 45 thickness steps were chosen between 0.001 mm and 0.2 mm. For thicknesses up to 1 mm, a constant step equal to 0.018 mm was adopted. The total number of spectral signatures for each radionuclide is equal to 90. For each simulated spectral signature, the total number of emitted γ-rays is around 100 million.

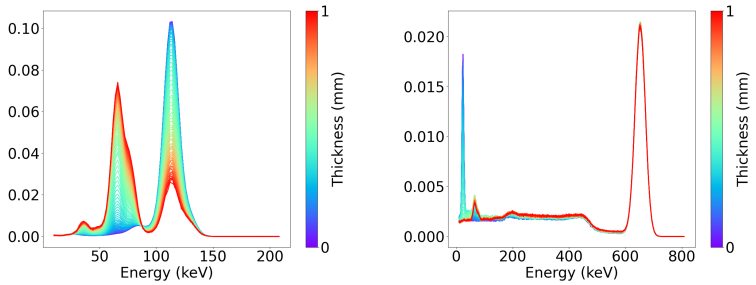

Fig. 2. Evolution of the simulated spectral signatures of ^{57}Co (left) and ^{137}Cs (right) as a function of lead thickness. The y-axis represents normalized amplitudes. The blue curves correspond to low thicknesses and the red curves correspond to high thicknesses. A new peak appears corresponding to X_K fluorescence photons having energies between 70 and 90 keV.

3. Interpolating autoencoder: modeling of spectral signatures

3.1. IAE: a trainable model to account for the spectral signature deformations

The objective is to build a surrogate or generative model to describe the deformations of the spectral signatures parameterized by the thickness of the shielding sphere surrounding the radioactive source. From a mathematical point of view, spectral signatures are signals that live on a 1-dimensional manifold that describes the relationship between the sphere thickness and the resulting spectral signature. Thus, designing a surrogate model boils down to building a model that generates spectral signatures belonging to this manifold. However, since no analytical model is available, this paper proposes resorting to a ML approach to learn the aforementioned manifold.

In the ML literature, learning a surrogate model for signals that live on a low-dimensional manifold can be done with autoencoders. In a nutshell, autoencoders are trainable models composed of a forward mapping called encoder that projects the data onto a low-dimensional latent domain. A second non-linear mapping, coined decoder, projects it back to the sample domain. As such, the decoder can be interpreted as a surrogate model for the spectral signatures with the latent domain as parameterization.

In the present article, a key limitation of standard autoencoders is that they require a large amount of training data. Furthermore, simulating spectral signatures with Geant4 is also computationally expensive, which limits the number of available samples for training. To alleviate this bottleneck, we make use of the IAE introduced in [12]. In brief, the IAE is composed of an extra component that performs linear interpolation from so-called anchor points in the latent domain. The advantage of the IAE is that it constrains the samples to be described as interpolants of anchor points that are known to be onto the physical manifold that describes the deformations of the spectral signatures. It has been advocated in [12] that this extra constraint allows training the IAE quite

efficiently when the training samples are scarce. This makes the IAE well-suited to build a surrogate model for the spectral signatures. In practice, the IAE is a neural network whose architecture is described in Fig. 3

More formally, let $\Phi : \mathbb{R}^M \to \mathbb{R}^D$ and $\Psi : \mathbb{R}^D \to \mathbb{R}^M$ be the encoder and the decoder, respectively. First, Φ encodes the input sample $s \in \mathbb{R}^M$ and the chosen anchor points $\{\varphi_a\}$ in the code domain. Let $\mathbf{\Omega} = [\Phi(\varphi_1) \cdots \Phi(\varphi_d)]$ be the matrix formed by encoded anchor points. Then, the code of input sample $\Phi(s)$ is approximated by its projection onto the affine hull of the encoded anchor points (see [12]). This is equivalent to approximating each sample on the code domain as a linear interpolation or barycenter of the encoded anchor points :

$$\begin{aligned} P_{aff(\mathbf{\Omega})}(s) = \mathbf{\Omega}\lambda = \sum_a \lambda_a \Phi(\varphi_a) \approx \Phi(s) \quad \text{with} \quad \lambda = Argmin_{\lambda \in S_d} \|\mathbf{\Omega}\lambda - \Phi(s)\|_2^2 \\ = \mathbf{\Omega}^+ \mathbf{\Phi(s)} + \frac{\mathbf{1} - \mathbf{1}^\top \mathbf{\Omega}^+ \mathbf{\Phi(s)}}{\mathbf{1}^\top \left(\mathbf{\Omega}^\top \mathbf{\Omega}\right)^{-1} \mathbf{1}} \left(\mathbf{\Omega}^\top \mathbf{\Omega}\right)^{-1} \mathbf{1} \end{aligned} \tag{1}$$

where S_d represents the simplex space: $\lambda \in S_d$ means that the sum of λ equals one. Finally, Ψ decodes the barycenter into the sample domain. The encoder and decoder are defined as trainable models with parameters θ, whose architecture will be specified later. Given a training dataset $\mathcal{T} = \{s_i\}_{i=1,\dots,T}$, the encoder and decoder are trained to minimize the reconstruction error of the input samples and the error between the codes of the input sample and their barycenters:

$$\mathcal{L}(\theta) = \sum_{s_i \in \mathcal{T}} \|s_i - (\Psi_\theta \circ P_{aff(\mathbf{\Omega})} \circ \Phi_\theta)(s_i)\|_2^2 + \mu \sum_{s_i \in \mathcal{T}} \|\Phi_\theta(s_i) - (P_{aff(\mathbf{\Omega})} \circ \Phi_\theta)(s_i)\|_2^2 \tag{2}$$

where μ is the parameter that controls the trade-off between two errors.

Once the model has been learned, the IAE can be used as a generative model. The input sample can be estimated as decoding of a linear interpolation of the encoded anchor points. In other words, the sample domain $\mathcal{M}$ can be approximated as a domain generated by a known function of a latent variable λ: $\mathcal{M} \approx \{\Psi(\mathbf{\Omega}\lambda); \lambda \in S_d\}$. Hence, the spectral signatures can be modeled via very low-dimensional variables for our application.

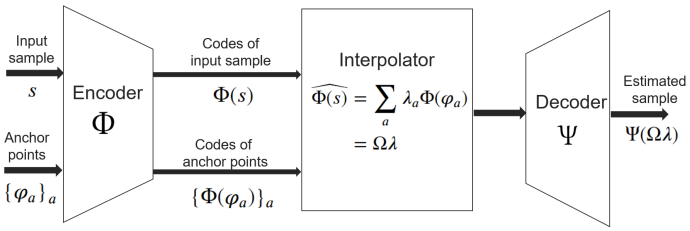

Fig. 3. Diagram of IAE

3.2. Individual IAE-based spectral signature model

This section describes the case when a different IAE model is independently trained for each radionuclide. The architecture of the model depends on the architectures of the encoder and decoder as well as the choice and number of anchor points that constrain the dimensionality of the model. Mathematically, the number of anchor points depends on the actual dimension of the physical manifold that describes the spectral variability. Since the spectral deformations are only related to the thickness of the sphere surrounding the radioactive source, they depend only on a single parameter. As advocated in [12], the number of anchor points should be at least equal to 2.

Several types of neural networks such as MLP or CNN have been investigated to build IAE models, and in our case, CNN better captures the structure and variability of spectral signatures. Consequently, the encoder and decoder architecture is based on CNN in this paper. More precisely, the encoder consists of L layers: each has a 1D convolution layer to get useful information (peaks, attenuation, ...), batch normalization to help train faster and in a more stable manner, and an activation function f. The decoder has the same structure, instead of using the 1D Convolution, ConvTranspose1d is used. Fig. 4 summarizes the architecture of the proposed IAE. The general IAE structure is the same for all radionuclides. However, the number of filters, the filter size and the stride in the convolution layers are different. The filter size and number of filters were chosen in ascending order according to layer. For each layer, the filter size was tested between 2 and 10, and the number of filters was selected between 10 and 30. The number of layers was chosen using the following method: adding new layers until the cost function of the training set does not improve significantly. Different hyperparameter values were investigated, and the best hyperparameters among them were chosen for each IAE model associated with each radionuclide. The input spectral signature's length depends on the maximum energy of emitted γ-photons of each radionuclide. For instance, the maximum value for ^{57}Co is 200 keV and 1600 keV for ^{60}Co. The IAE model for each radionuclide is only trained on this energy interval to improve learning.

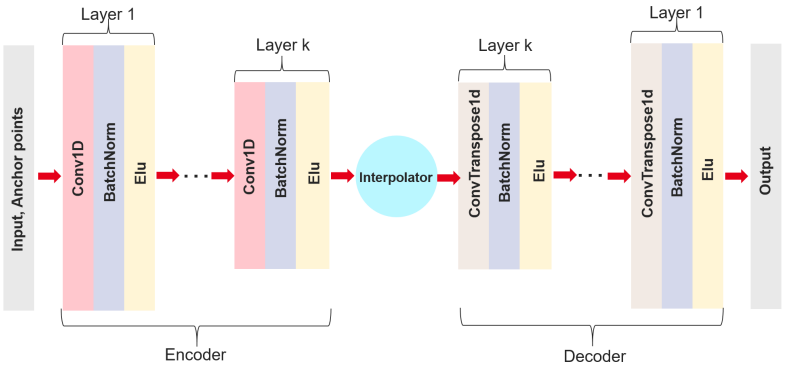

Fig. 4. Architecture of the proposed IAE model

3.3. Joint IAE-based spectral signature model

This section describes a more realistic case corresponding to several radionuclides placed in the same source housing with regard to the material and the thickness. This configuration yields a correlation between the variation of the spectral signatures of all radionuclides and the sphere thickness. Since the IAE model is trained to capture the spectral variability, the latent domain describes how they evolve when the thickness changes. In that context, one IAE model is needed to encode this information in a single joint latent domain for all the radionuclides. Therefore, the previous IAE model is extended to be simultaneously trained for all radionuclides to share the same latent space. In other words, the same parameter λ allows describing all the spectral signatures at once. This modification is particularly advantageous as it allows accounting for the correlations between the deformations of spectral signatures for all radionuclides from a single low-dimensional space. In this setting, an input sample is defined by the whole of the spectral signatures of all radionuclides. The IAE structure is almost the same as described before. For the first hidden layer of the encoder, the individual model has a filter depth of 1 and the joint model has a depth of the number of radionuclides. The same applies to the last layer of the decoder. All other layers remain unchanged.

3.4. Numerical evaluation of the IAE models

The accuracy of both IAE models described above was assessed using the dataset described in Section 2.1 (steel sphere) for the training and testing data. The IAE code was built by means of the open-source Pytorch [13] library on Python. The implementation and the hyperparameters of the IAE models are described in Appendix A. For each radionuclide, 71 spectral signatures were randomly selected for training and the remaining 25 were for testing. As already mentioned, the manifold size is one (steel thickness), so two anchor points are required for this dataset. The associated spectral signatures correspond to the

smallest (1 μm) and largest thickness (30 mm). For this application, another positivity constraint was also added to the latent variable λ. With this constraint, λ is defined in $[0,1] \times [0,1]$ instead of $\mathbb{R} \times \mathbb{R}$. This constraint enables a fast and efficient search for the λ value when using the IAE as a generative model. It is also easy to interpret the λ value in this case: when λ of an anchor point is close to 1, the spectral signature is very similar to that anchor point.

The normalized mean square error (NMSE) is applied to assess the reconstruction performance of the estimated spectral signatures:

$$\mathrm{NMSE}(s, \hat{s}) = -10 \log \frac{\sum_m (s_m - \hat{s}_m)^2}{\sum_m (s_m)^2} \tag{3}$$

where $\hat{s}$ is the estimator of s. The NMSE of the spectral signature reconstructed by the IAE model was calculated for each spectrum in the test dataset for each radionuclide. Table 1 shows that both IAE models accurately estimate the spectral signatures: the NMSE median ranges between 34 and 40 dB for all radionuclides. In addition, it is noteworthy that the first and third quartiles are close to the median. Fig. 5 illustrates a ^{133}Ba spectral signature estimated by individual and joint IAE models with the lowest NMSE ($\approx$ 33 dB). It can be highlighted that the spectral signatures reconstructed by the two IAE models are very similar to the Geant4 simulation with very low residuals.

In order to use these IAE models within an unmixing algorithm, it is also important to evaluate their robustness to perturbations such as noise. To this end, the accuracy of the proposed IAE models was assessed with respect to additive Gaussian perturbations: Gaussian noise with different signal-to-noise ratios (SNR) was added to the test dataset. To recover the original spectral signatures, the IAE was used as a generative model. The value of λ was estimated to obtain the spectral signature of each radionuclide closest to the noisy spectrum s for the individual model or the spectral signatures of all radionuclides closest to the noisy spectra s for the joint model using the following formula:

$$\hat{\lambda} = Argmin_{\lambda \in S_d^+} \|\Psi(\mathbf{\Omega}\lambda) - s)\|_2^2$$

It can be interpreted as the orthogonal projection onto the space generated from the latent variable λ. The following constraints on λ are essential to ensure that the IAE model does not generate incorrect spectral signatures: λ is positive and the sum of λ is equal to one. To consider these constraints, SLQSP from Scipy [14] was used to solve this problem. The SLSQP optimizer is a sequential least squares programming algorithm that replaces the original problem with a sequence of quadratic problems and transforms it into a least squares problem.

To assess the denoising performance, the NMSE was calculated using the original spectral signatures without noise for both IAE models with different SNR values. Fig. 6 shows the evolution of NMSE of the four radionuclides as a function of SNR. When the noise is low (high SNR), both models recover well the original signatures with NMSE larger than 33 dB. When the noise is significant, the joint model outperforms the individual model. This result is due to the fact that the joint model shares the same λ for all radionuclides, unlike

the individual model. The individual model independently searches for spectral signatures close to the noisy signatures of each radionuclide so it can be easily influenced by noise. In addition, when one radionuclide is well estimated, the joint model can also improve the estimation of other radionuclides, which the individual model cannot do.

	^{60}Co	^{133}Ba	^{57}Co	^{137}Cs
Ind	**34.0** [33.1, 34.7]	**36.2** [35.3, 36.8]	**39.6** [35.5, 42.9]	**36.6** [35.0, 38.2]
Joint	**34.5** [34.2, 35.0]	**36.2** [35.3, 36.9]	**36.4** [35.2, 38.6]	**36.1** [35.4, 37.5]

Table 1: NMSE (dB) of estimated spectral signatures for all radionuclides for the test dataset. Each row is the result of each IAE model. Ind stands for individual IAE-based model, and Joint stands for joint IAE-based model. The values in each cell are the median, 25th percentile and 75th percentile, respectively.

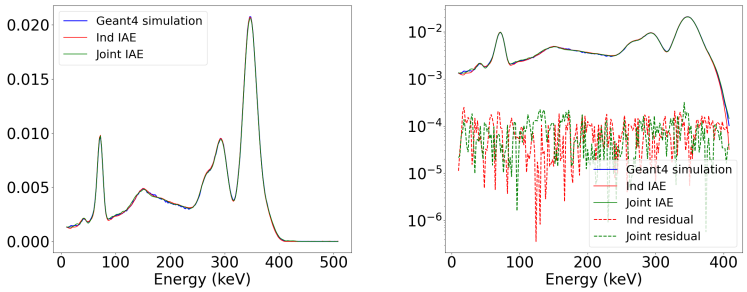

Fig. 5. An example of ^{133}Ba spectral signature estimated by individual IAE (red curve) and by joint IAE (blue curve) with the lowest NMSE ($\approx$ 33 dB) (left) and their residuals (right).

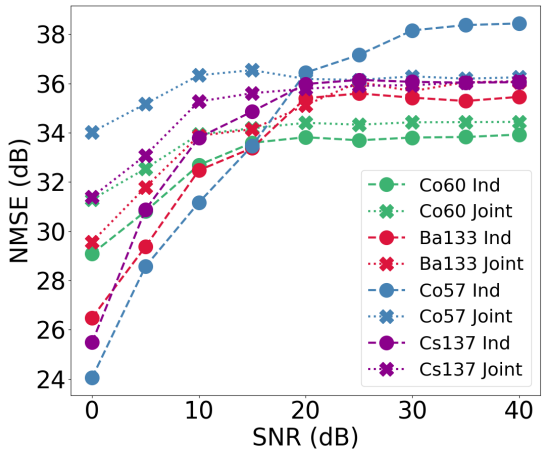

Fig. 6. Mean NMSE of estimated spectral signatures on test dataset as a function of SNR for all radionuclides. Ind stands for the individual IAE-based model, and Joint stands for the joint IAE-based model. The dotted lines (symbol O) are those of the individual model, and the crossed lines (symbol X) correspond to the joint model.

4. Semi-blind Spectral unmixing (SEMSUN)

In this part, the IAE models are included in an unmixing procedure to implement a joint estimation of the spectral signatures and the counting vector from an observed spectrum. To this end, a novel hybrid unmixing algorithm is developed by combining the IAE models with Poisson statistics. Two versions of the algorithm are presented, corresponding to the two IAE models described previously.

An observed spectrum $y = [y_1, ..., y_M]$ consists of M channels corresponding to energy intervals deposited in a detector sensitive to γ-photons. The counting in each channel y_m is the number of events for a given energy interval. Let $X \in \mathbb{R}_+^{M \times N}$ be a matrix such that each column X_i is the normalized spectral signature of each radionuclide. In this work, the natural background (Bkg) is an element of X, similar to the radionuclides. Its mixing weight or counting will be estimated during the unmixing procedure. The observed spectrum y follows the Poisson distribution of $Xa : y \sim \mathcal{P}(Xa)$ where a is the vector containing the mixing weights of each radionuclide.

The statistical independence of measurement yields the following joint probability for the likelihood:

$$P(y|X,a) = \prod_{m=1}^{M} \frac{(Xa)_m^{y_m} e^{(Xa)_m}}{y_m!} \tag{4}$$

The negative log-likelihood (cost function) has the following formula:

$$L(a, X) = \sum_{m=1}^{M} ((Xa)_m - y_m log((Xa)_m)) \tag{5}$$

Minimizing the negative log-likelihood is equivalent to minimizing the divergence:

$$D(y||Xa) = \sum_{m=1}^{M} ((Xa)_m - y_m + y_m log(y_m) - y_m log((Xa)_m)) \tag{6}$$

In the present work, the joint estimation of the matrix X and the vector a from the observed spectrum y is expressed as follows:

$$\hat{X}, \hat{a} = Argmin_{X,a} \sum_{i=2}^{p} \chi_{\phi_i}(X_i) + \chi_{(.\geq 0)}(a) + D(y||Xa) \tag{7}$$

where $\chi_{(.\geq 0)}(a)$ represents the positivity constraint on the vector a (i.e., vector with non-negative elements). $\chi_{\phi_i}(X_i)$ represents the constraint for each radionuclide: the spectral signature must be the decoding of the linear interpolation of the encoded anchor points.

$$\chi_{\phi_i}(X_i) = \begin{cases} 0 & \exists \lambda \in S_d^+ : X_i = \Psi(\mathbf{\Omega}\lambda) \\ +\infty & \text{otherwise.} \end{cases}$$

i starts from 2 because the first column of the matrix X is Bkg and it is known, so we do not need to estimate it.

The problem is non-convex, but assuming that the problem is multi-convex (i.e., convex when a or X is fixed), it can be solved by the Block coordinate descent (BCD) algorithm [15]. The main idea behind this algorithm is to divide the problem into several blocks. For each block, a single parameter is estimated, while the other parameters are fixed.

4.1. Semi-blind Spectral unmixing based on individual manifold learning (SEMSUN-i)

The individual IAE model can be used to define constraints on spectral signatures. $N-1$ IAE models are trained to independently learn the shape and variability of spectral signatures of $N-1$ radionuclides. In this case, BCD is used with N blocks: the first block estimates the vector a, and the i^{th} block estimates the spectral signature of the i^{th} radionuclide. All blocks are executed consecutively until the algorithm converges. It should be highlighted that this algorithm is effective when the radionuclides come from different source housing. For instance, in our case, the thickness of the sphere may be different for each radionuclide.

In detail, at iteration $k+1$ for the first block, the non-negative vector a^{k+1} is estimated by minimizing the cost function when the matrix X^k is fixed:

$$a^{k+1} = Argmin_a \chi_{(.\geq 0)}(a) + D(y||X^k a) \tag{8}$$

Several algorithms are proposed to solve this problem, such as the multiplicative update algorithm NNPU [6] or the Chambolle-Pock algorithm [7]. In this work, the NNPU is applied since it is faster.

Let: $X^{k,i} = (X_{Bkg}, X_{<i}^{k+1}, X_i^k, X_{>i}^k)$ and $z_i = X^{k,i}a^{k+1} - X_i^k a_i^{k+1}$. For the i^{th} block, the estimated spectral signature of i^{th} radionuclide minimizes the cost function and satisfies the constraint based on the IAE model:

$$X_i^{k+1} = Argmin_{X_i} D(y||z_i + X_i a_i^{k+1}) + \chi_{\phi_i}(X_i) \tag{9}$$

The change of variable on X_i is performed to solve this problem:

$$X_i^{k+1} = \Psi(\mathbf{\Omega}\hat{\lambda}) \quad with \quad \hat{\lambda} = Argmin_{\lambda \in S_d^+} D(y||z_i + \Psi(\mathbf{\Omega}\lambda)a_i^{k+1})) \tag{10}$$

It turns into finding the spectral signature generated by the IAE model that minimizes the cost function. It should be noted that using the IAE model to constrain spectral signatures is equivalent to using the IAE model as a generative model for our application. The SLQSP solver [14] discussed in 3.4 is applied to tackle this problem. The stopping criterion is either the relative error on the spectral signatures X and on the counting a is lower than a predefined value (by default $1e^{-6}$), or the number of iterations is higher than the maximum number of iterations (by default 200). The initial values of the spectral signatures are provided by the user.

while *stopping criterion is not valid* **do**
  1. Update **a**

$$a^{k+1} = Argmin_a \chi(. \geq 0)(a) + D(y||X^k a)$$

  while *stopping criterion is not valid* **do**

$$a^{k+1} = a^k \odot ((X^k)^T \frac{y}{X^k a^k})$$

  end
  2. Update $\mathbf{X_i}$ **for** *i =2..N* **do**
  :

$$X^{k,i} = (X_{Bkg}, X_{<i}^{k+1}, X_i^k, X_{>i}^k)$$

$$z_i = X^{k,i}a^{k+1} - X_i^k a_i^{k+1}$$

$$X_i^{k+1} = Argmin_{X_i} D(y||z_i + X_i a_i^{k+1}) + \chi_{\phi_i}(X_i)$$

$$X_i^{k+1} = \Psi(\mathbf{\Omega}\hat{\lambda}) \quad with \quad \hat{\lambda} = Argmin_{\lambda \in S_d^+} D(y||z_i + \Psi(\mathbf{\Omega}\lambda)a_i^{k+1})$$

  end
end

Algorithm 1: Pseudocode of the SEMSUN-i algorithm

4.2. Semi-blind Spectral unmixing based on joint manifold learning (SEMSUN-j)

When all radionuclides are in the same source housing, the joint IAE model is better suited. In this case, a single IAE model can capture the variability of spectral signatures of all radionuclides. The BCD algorithm is therefore applied according to two blocks: one for a and one for X. The first block is identical to the previous case. The second block estimates the spectral signatures of all radionuclides X from the observed spectrum y and the known counting vector a:

$$X^{k+1} = \Psi(\mathbf{\Omega}\hat{\lambda}) \quad with \quad \hat{\lambda} = Argmin_{\lambda \in S_d^+} D(y||X_{Bkg}a_1^{k+1} + \Psi(\mathbf{\Omega}\lambda)a_{i>1}^{k+1}) \quad (11)$$

Detailed implementation is identical to that described above. As mentioned previously, the joint model searches for a single λ for all radionuclides instead of having a different λ value for each radionuclide. Calculation time is therefore shorter than in the individual case. It is noteworthy that for both algorithms, convergence is not theoretically guaranteed. The assumption that, when a is fixed, the cost function is convex on X for the joint model or X_i for the individual model is not theoretically proven, as the IAE model is non-linear.

while *stopping criterion is not valid* **do**

1. Update **a**

$$a^{k+1} = Argmin_a \chi(. \geq 0)(a) + D(y||X^k a)$$

while *stopping criterion is not valid* **do**

$$a^{k+1} = a^k \odot ((X^k)^T \frac{y}{X^k a^k})$$

end

2. Update **X**

$$X^{k+1} = Argmin_X \sum_{i=2}^{p} \chi_{\phi_i}(X_i) + D(y||Xa^{k+1})$$

$$X^{k+1} = \Psi(\mathbf{\Omega}\hat{\lambda}) \quad with \quad \hat{\lambda} = Argmin_{\lambda \in S_d^+} D(y||X_{Bkg}a_1^{k+1} + \Psi(\mathbf{\Omega}\lambda)a_{i>1}^{k+1})$$

end

Algorithm 2: Pseudocode of the SEMSUN-j algorithm

5. Numerical evaluation of spectral unmixing of the hybrid algorithms

This section assesses the estimated spectral signatures and counting obtained with the two hybrid algorithms described above. The numerical evaluation was performed with simulated γ-spectra at high and low statistics using the two datasets presented in Section 2. The results were compared to the non-negative joint estimation of X and a without any additional constraint carried

out by means of the Non-negative Matrix Factorization (NMF) [16] with the same initialization value as for the two hybrid algorithms. The comparison was also carried out when the spectral signatures X are known using the NNPU algorithm to estimate the counting vector a. It can be interpreted as the best possible result that can be achieved. It is thus defined as Oracle in the following. NMSE was used to compare the estimated spectral signatures of all algorithms to assess the result of the unmixing procedure. The most poorly estimated spectral signatures (low NMSE) were mainly studied. Consequently, the median, 25th and 5th percentile NMSE were calculated from all simulated γ-spectra. For the estimated counting vector, relative errors were analyzed for all radionuclides, and boxplot was applied to illustrate their distributions. The estimated spectral signatures can be visualized using the estimated latent variable λ distribution. The two anchor points were used with the simplex constraint on λ, so the dimension of λ equals one. All λ values of the first anchor point of all simulated γ-spectra were sorted in ascending order. The spectral signature corresponding to the α percentile is the spectral signature generated by the IAE model with the λ value at the α percentile. The variability of estimated signature between the α and $1-\alpha$ percentiles is the envelopes of the spectral signature at the α and $1-\alpha$ percentiles.

5.1. Attenuation and Compton scattering effects in a steel sphere

The IAE models developed in Section 3.4 were used to learn the deformations of spectral signatures due to attenuation and Compton scattering with the dataset of the steel sphere in Section 2.1. The numerical eveluation was performed using γ-spectra simulated according to the following settings:

- A mixture of the natural background Bkg and four radionuclides (^{57}Co, ^{60}Co, ^{133}Ba and ^{137}Cs) with the corresponding mixing weights: 0.5, 0.08, 0.2, 0.12 0.1.
- The theoretical spectral signatures to be estimated correspond to a thickness of 5.2 mm of steel sphere.
- The initial spectral signatures correspond to a thickness of 0.001 mm.
- Two scenarios were considered for the full-spectrum total counting: high statistics with an average counting of 100000 and low statistics with an average counting of 2500.
- For each scenario, 1000 MC simulated γ-spectra with Poisson statistics.

The theoretical and initial spectral signatures used to evaluate the joint estimation are displayed in Fig. 7. Two examples of simulated spectra, each corresponding to high and low statistics, are given in Fig. 8.

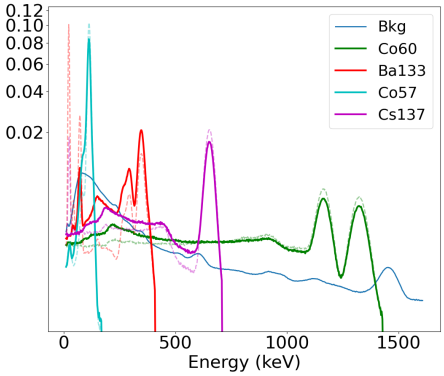

Fig. 7. Theoretical and initial spectral signatures. The continuous curves correspond to the theoretical spectral signatures, and the dashed curves correspond to the initial spectral signatures.

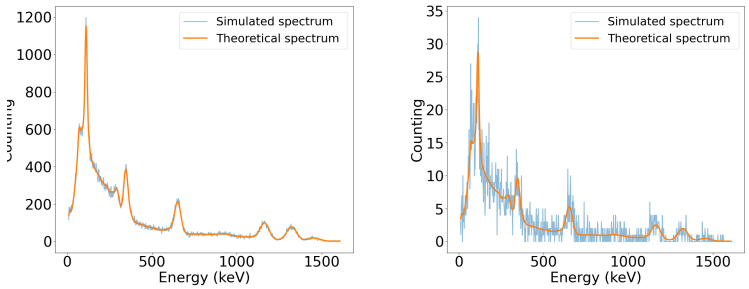

Fig. 8. Simulated and theoretical spectrum at high statistics (left): average total counting of 100 000 and at low statistics (right): average total counting of 2500 .

Table 2 shows the NMSE of the estimated spectral signatures for all radionuclides in the case of the high-statistics evaluation. As expected, the spectral signatures are poorly estimated when using NMF, with very low NMSE values (the median is less than 15 dB) due to the absence of constraints on spectral signatures. In this case, the problem is ill-posed, and, as a result, the estimated spectral signatures are highly dependent on the initial spectral signatures. With SEMSUN-i, the spectral signatures are better estimated, with the median of NMSE over 28 dB for all radionuclides. Of all three algorithms, SEMSUN-j estimates spectral signatures most accurately, with 95% of the NMSE over 29.4 dB. As demonstrated above, the two hybrid algorithms efficiently recover the

spectral signature of all radionuclides at high statistics. Fig. 9 and Fig. 10 display the estimated spectral signatures by SEMSUN-i and SEMSUN-j for ^{60}Co and ^{133}Ba.

Table 3 shows the relative errors of the estimated counting for the four algorithms at high statistics. Oracle represents the result when the spectral signatures are known. The estimated counting of NMF is significantly different from the expected values due to the poor estimation of the spectral signatures. SEMSUN-i provides a satisfactory estimation of counting for natural background Bkg, ^{133}Ba and ^{57}Co, with a relative error distribution not significantly different compared to Oracle. For ^{137}Cs and ^{60}Co, the relative error is about three times greater than the result of Oracle. This outcome can be interpreted as a consequence of the lower precision of the spectral signatures estimated by SEMSUN-i for these radionuclides. Regarding the results of SEMSUN-j, the error distribution is similar to Oracle: the counting obtained by estimating spectral signatures is almost the same as in the case where spectral signatures are known.

	^{60}Co	^{133}Ba	^{57}Co	^{137}Cs
SEMSUN-i	**30.8** |27.8, 24.4|	**33.2** |30.1, 26.1|	**36.9** |33.0, 28.2|	**28.2** |23.8, 20.0|
SEMSUN-j	**34.5** |33.8, 32.2|	**35.2** |32.8, 29.4|	**38.3** |37.6, 36.1|	**37.5** |35.8, 33.0|
NMF	**10.1** |9.9, 9.7|	**7.1** |7.0, 6.7|	**14.8** |14.4, 14.0|	**6.8** |6.6, 6.4|

Table 2: High-statistics results: NMSE (dB) of estimated spectral signatures of all algorithms for all radionuclides. Each row represents the result of each algorithm. The values in each cell are the median, 25th percentile, and 5th percentile, respectively.

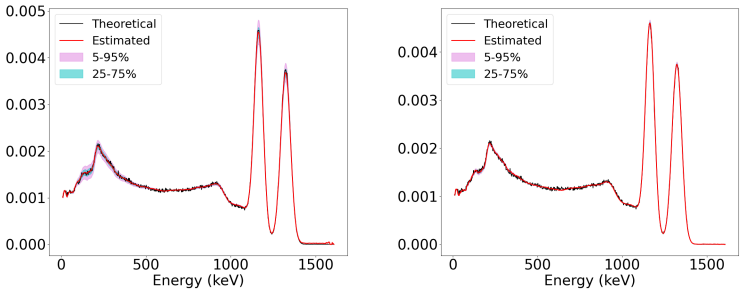

Fig. 9. High-statistics results: ^{60}Co spectral signatures estimated by SEMSUN-i (left) and SEMSUN-j (right). Theoretical represents the theoretical spectral signature, and Estimated represents the average of the estimated spectral signatures for all MC simulated γ-spectra. 25-75 % represents the interval between the 25 and 75 percentile. Same for 5-95%.

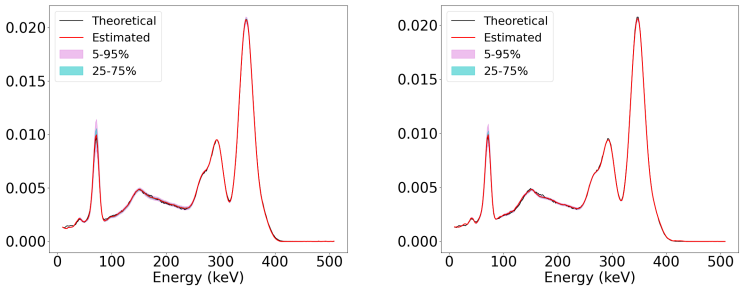

Fig. 10. Same as Fig. 9 with ^{133}Ba

	Bkg	^{60}Co	^{133}Ba	^{57}Co	^{137}Cs
SEMSUN-i	**-0.4** [-1.3, 0.4]	**0.6** [-1.4, 2.8]	**0.6** [-1.1, 2.0]	**-0.1** [-1.5, 1.6]	**0.3** [-3.9, 4.5]
SEMSUN-j	**0.0** [-0.7, 0.8]	**-0.6** [-1.4, 0.4]	**0.1** [-1.3, 1.5]	**0.3** [-0.9, 1.9]	**0.5** [-0.8, 2.0]
Oracle	**0.0** [-0.6, 0.6]	**-0.0** [-0.9, 0.8]	**0.1** [-1.3, 1.5]	**-0.1** [-1.3, 1.4]	**-0.0** [-1.4, 1.3]
NMF	**-50.5** [-52.8, -48.3]	**26.8** [25.1, 28.6]	**37.6** [35.3, 39.9]	**63.2** [60.5, 66.2]	**103.5** [100.3, 106.8]

Table 3: High-statistics results: relative errors of estimated counting (%) of all algorithms for all radionuclides. Each row represents the result of each algorithm. The values in each cell are the median, 25th percentile and 75th percentile, respectively.

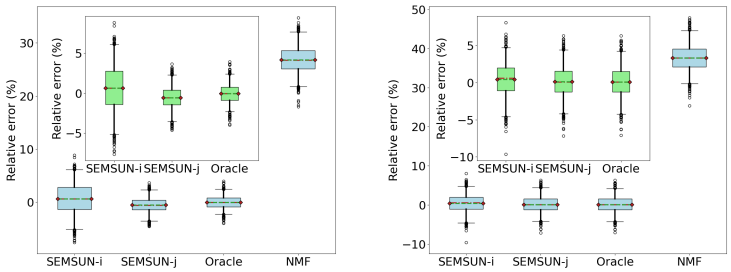

Fig. 11. High-statistics results: relative errors of estimated counting of ^{60}Co (left) and ^{133}Ba (right). Oracle stands for the result when the spectral signatures matrix is known. In the boxplot center, the red line is the median, and the blue line is the mean. The box is composed of the first and third quartiles. The whiskers represent the 2nd percentile and 98th percentile of the data. A sub-figure shows a zoom on the results of the first three algorithms.

At low statistics, Table 4 provides the NMSE of the estimated spectral signatures for all radionuclides. Basically, the conclusion is similar to in the case of high statistics. NMF estimates spectral signatures poorly: the median is less than 4 dB for all radionuclides, except for ^{57}Co, which is less than 10.3 dB. The SEMSUN-i result is better but the NMSE values are relatively low for all

radionuclides, particularly for ^{137}Cs. The highest accuracy on estimated spectral signatures is obtained with SEMSUN-j, but the NMSE results are lower than in the case of high statistics due to the higher noise level of simulated γ-spectra. The estimated ^{133}Ba spectral signature by SEMSUN-j is less accurate than that of the other radionuclides because the ^{133}Ba spectral signature is more sensitive to the steel thickness. Fig. 12 and Fig. 13 display the estimated spectral signature with the SEMSUN-i and SEMSUN-j algorithms. For ^{137}Cs, in some cases, the spectral signatures estimated by the SEMSUN-i show the low-energy X-ray peak corresponding to spectral signatures related to low thicknesses that is not present in the theoretical spectral signature (see Fig. 13). In the case of SEMSUN-j, the shape of the spectral signatures is better estimated; in particular, the low-energy x-ray peak is not present. This improvement can be explained by the fact that the joint IAE-based model constrains the spectral signature from the same thickness, unlike the individual IAE-based model. Fig. 14 shows the relative errors of the estimated counting for four algorithms. SEMSUN-j's result is better than SEMSUN-i's and similar to Oracle's.

	^{60}Co	^{133}Ba	^{57}Co	^{137}Cs
SEMSUN-i	**18.4** |13.7, 11.9|	**19.7** |15.1, 10.0|	**21.6** |16.5, 12.0|	**14.1** |11.1, 8.6|
SEMSUN-j	**28.5** |24.1, 19.8|	**23.9** |19.1, 14.6|	**32.6** |28.7, 24.6|	**27.6** |22.8, 18.4|
NMF	**2.2** |2.0, 1.8|	**3.9** |3.5, 2.9|	**10.3** |9.6, 8.7|	**3.5** |3.2, 2.9|

Table 4: Low-statistics results: NMSE (dB) of estimated spectral signatures of all algorithms for all radionuclides. The values in each cell are the median, 25th percentile, and 5th percentile, respectively.

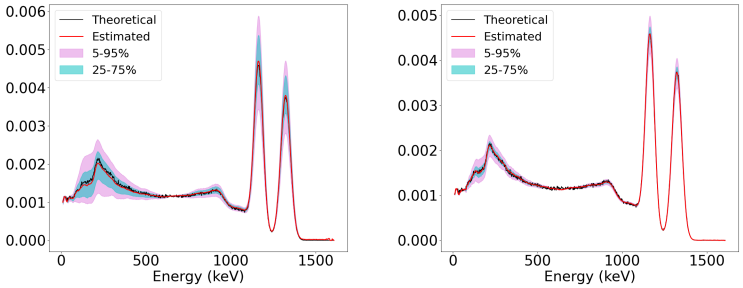

Fig. 12. Low-statistics results: ^{60}Co spectral signatures estimated by SEMSUN-i (left) and SEMSUN-j (right). Theoretical represents the theoretical spectral signature, and Estimated represents the average of the estimated spectral signatures for all MC simulated γ-spectra. 25-75 % represents the estimated signature between the 25 and 75 percentile. Same for 5-95%.

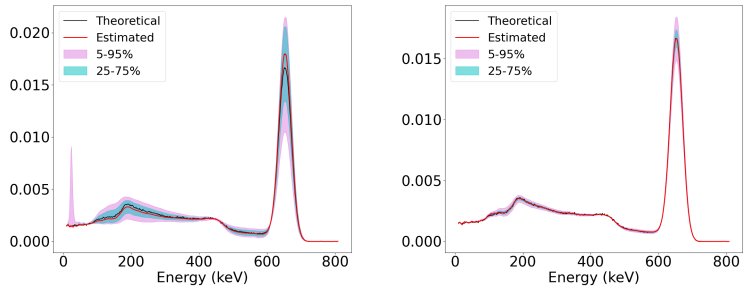

Fig. 13. Same as Fig. 12 with ^{137}Cs

	Bkg	^{60}Co	^{133}Ba	^{57}Co	^{137}Cs
SEMSUN-i	**-1.6** [-6.9, 4.0]	**-1.9** [-11.6, 9.4]	**1.1** [-8.0, 10.5]	**-0.6** [-10.4, 9.9]	**1.8** [-16.3, 24.7]
SEMSUN-j	**-0.4** [-4.5, 4.2]	**-0.3** [-6.3, 5.3]	**0.5** [-7.7, 8.7]	**0.2** [-8.6, 10.0]	**0.3** [-8.2, 9.3]
Oracle	**0.2** [-3.5, 4.0]	**-0.5** [-5.3, 4.5]	**-0.2** [-8.1, 8.2]	**-0.6** [-9.1, 8.8]	**-0.5** [-8.4, 7.8]
NMF	**-100.0** [-100.0, -100.0]	**67.7** [63.9, 71.7]	**83.8** [78.6, 88.9]	**119.1** [111.1, 126.7]	**168.1** [162.5, 173.8]

Table 5: Low-statistics results: relative errors of estimated counting (%) of all algorithms for all radionuclides. The values in each cell are the median, 25th percentile and 75th percentile, respectively.

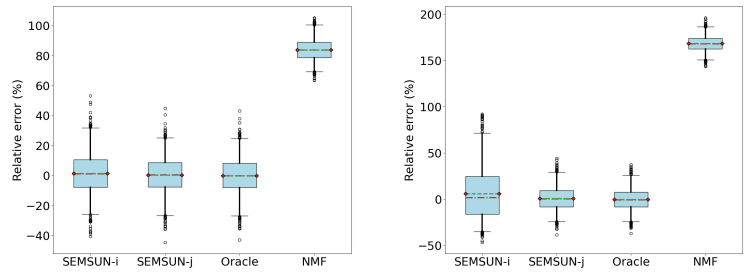

Fig. 14. Low-statistics results: relative errors of estimated counting of ^{133}Ba (left) and ^{137}Cs (right). Oracle stands for the result when the spectral signatures matrix is known. In the boxplot center, the red line is the median, and the blue line is the mean. The box is composed of the first and third quartiles. The whiskers represent the 2nd percentile and 98th percentile of the data.

5.2. Fluorescence, attenuation and Compton scattering effects in a lead sphere

In this part, the numerical evaluation is extended to the dataset corresponding to simulated spectra with the lead sphere in Section 2.2 that considers the deformations of spectral signatures due to fluorescence, attenuation and Compton scattering. The IAE models were trained using this dataset with the same

hyperparameters given in Appendix A. The numerical evaluation was carried out in the same manner as described in the previous section. The theoretical spectral signatures to be estimated correspond to a thickness of 0.5 mm of lead sphere. Fig. 15 displays the theoretical and simulated spectrum at high and low statistics. Table 6 and Table 7 show the NMSE of the estimated spectral signatures and the relative errors of estimated counting for all radionuclides at high statistics. SEMSUN-j accurately estimates the spectral signature of all radionuclides, and the estimated counting is similar to the results of Oracle.

At low statistics, Table 8 shows the NMSE of the estimated spectral signatures for all radionuclides. The SEMSUN-j algorithm leads to improved results compared to the SEMSUN-i algorithm, except for ^{57}Co. The spectral signatures are well recovered for ^{60}Co and ^{137}Cs, whose variability with lead thickness is less critical compared to the other radionuclides. For ^{133}Ba and ^{57}Co, the peaks are in the low-energy range, with significant noise due to the contribution of natural background and Compton scattering from the other radionuclides. As a result, the estimated spectral signatures for these radionuclides are less accurate as they fit the noise. For the estimated counting shown in Table 9, the results of the SEMSUN-j algorithm for ^{60}Co and ^{137}Cs are close to those given by Oracle. In the case of ^{133}Ba and ^{57}Co, the interval between the first and third quartile of the estimated counting is slightly larger than that of Oracle due to the less accurate estimation of their spectral signature. Compared with the numerical evaluation with steel sphere, the results at low statistics are slightly less accurate for ^{133}Ba and ^{57}Co because the shape of their spectral signatures is more sensitive to the lead thickness due to the fluorescence effect.

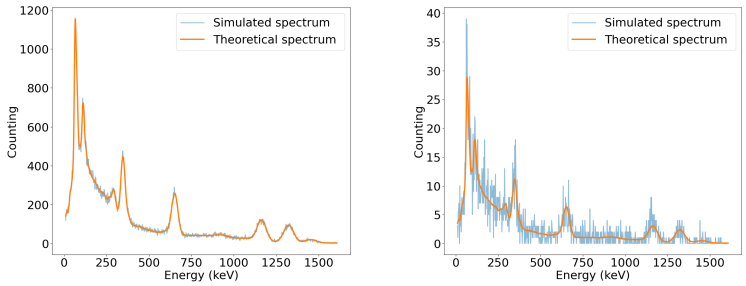

Fig. 15. Simulated and theoretical spectrum with high statistics: average total counting of 100 000 (left) and with low statistics: average total counting of 2500 (right)

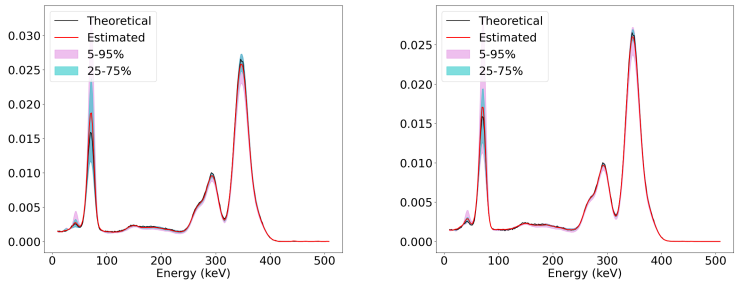

Fig. 16. ^{133}Ba spectral signature estimated by SEMSUN-i (left) and SEMSUN-j (right). Theoretical stands for the theoretical spectral signature, and Estimated represents the average of the estimated spectral signatures for all MC simulated γ-spectra. 25-75 % represents the estimated signatures between the 25 and 75 percentile. Same for 5-95%.

	^{60}Co	^{133}Ba	^{57}Co	^{137}Cs
SEMSUN-i	**29.7** |29.7, 28.9|	**30.6** |27.0, 22.3|	**32.6** |29.0, 24.7|	**33.3** |31.2, 28.5|
SEMSUN-j	**33.3** |33.2, 33.1|	**34.9** |31.9, 27.8|	**32.8** |28.9, 24.4|	**37.4** |37.3, 37.1|
NMF	**9.9** |9.7, 9.4|	**5.1** |5.0, 4.9|	**1.8** |1.8, 1.8|	**6.5** |6.3, 6.1|

Table 6: High-statistics results: NMSE (dB) of estimated spectral signatures of all algorithms for all radionuclides. The values in each cell are the median, 25th percentile, and 5th percentile respectively.

	Bkg	^{60}Co	^{133}Ba	^{57}Co	^{137}Cs
SEMSUN-i	**-0.3**[-0.9, 0.2]	**1.6**[0.6, 2.4]	**-0.5**[-2.0, 0.8]	**0.3**[-2.0, 2.4]	**-0.4**[-1.6, 0.7]
SEMSUN-j	**-0.0**[-0.6, 0.5]	**0.2**[-0.5, 0.9]	**0.8**[-0.5, 2.2]	**-0.4**[-2.4, 1.3]	**-0.7**[-1.9, 0.4]
Oracle	**0.0**[-0.5, 0.6]	**-0.1**[-0.7, 0.7]	**0.1**[-1.0, 1.2]	**0.3**[-1.4, 1.6]	**-0.0**[-1.2, 1.2]
NMF	**-51.9**[-54.1, -49.7]	**32.2**[30.6, 34.0]	**67.4**[65.1, 70.0]	**19.3**[16.7, 21.6]	**99.0**[95.9, 102.1]

Table 7: High-statistics results: relative errors of estimated counting (%) of all algorithms for all radionuclides. The values in each cell are the median, 25th percentile and 75th percentile respectively.

	^{60}Co	^{133}Ba	^{57}Co	^{137}Cs
SEMSUN-i	**29.7** |29.7, 25.3|	**16.5** |13.2, 12.3|	**19.8** |15.2, 10.5|	**32.3** |25.6, 16.3|
SEMSUN-j	**33.0** |32.5, 31.0|	**21.9** |17.7, 13.1|	**18.3** |13.8, 8.4|	**36.4** |34.9, 31.4|
NMF	**2.4** |2.2, 1.9|	**4.0** |3.6, 3.2|	**1.3** |1.2, 1.0|	**3.6** |3.3, 2.9|

Table 8: Low-statistics results: NMSE (dB) of estimated spectral signatures of all algorithms for all radionuclides. The values in each cell are the median, 25th percentile, and 5th percentile respectively.

	Bkg	^{60}Co	^{133}Ba	^{57}Co	^{137}Cs
SEMSUN-i	**-0.5**[-4.0, 3.0]	**0.9**[-3.5, 5.5]	**-0.2**[-8.6, 8.5]	**1.5**[-9.9, 13.5]	**0.1**[-7.2, 6.4]
SEMSUN-j	**-0.2**[-3.5, 3.4]	**0.1**[-4.3, 4.2]	**0.8**[-7.4, 10.4]	**0.2**[-11.5, 11.3]	**-0.3**[-7.4, 6.2]
Oracle	**-0.1**[-3.4, 3.6]	**-0.2**[-4.4, 3.9]	**0.4**[-7.4, 7.6]	**0.8**[-8.4, 10.4]	**0.3**[-6.8, 6.7]
NMF	**-100.0**[-100.0, -100.0]	**72.2**[68.3, 75.8]	**116.7**[111.3, 121.8]	**69.5**[63.2, 75.9]	**160.7**[154.7, 166.5]

Table 9: Low-statistics results: relative errors of estimated counting (%) of all algorithms for all radionuclides. The values in each cell are the median, 25th percentile and 75th percentile respectively.

6. Conclusion

A hybrid semi-blind unmixing approach has been developed for automatic full-spectrum analysis of γ-spectra including spectral deformations due to physical effects such as attenuation, Compton scattering and fluorescence. Since no analytical model is available to describe these phenomena, a specific ML model named IAE was applied to capture these deformations when the training samples were scarce. The investigations were performed using Geant4 simulated spectral signatures of a NaI(Tl) detector for four radionuclides (^{57}Co, ^{60}Co, ^{133}Ba, ^{137}Cs) present in a radioactive point source enclosed in a sphere (steel, lead). Two IAE models have been studied: the individual model that learns independently for each radionuclide and a joint model that captures correlations between the spectral variability for all radionuclides. As shown in this article, both IAE models can effectively capture the variability of spectral signatures with a limited dataset of simulated γ-spectra (less than 100). The IAE models have been included in an unmixing procedure to jointly estimate the spectral signatures and counting of all radionuclides from a single observed spectrum. To this end, the hybrid unmixing algorithm based on the BCD algorithm has been developed to apply the IAE models to constrain the spectral signatures. The numerical evaluation was carried out using simulated mixtures with Poisson statistics of the four radionuclides mentioned above with an experimental natural background at high and low statistics. The estimated counting was compared to the case that the spectral signatures are known (Oracle). At high statistics, the hybrid algorithm enables precise estimation of spectral signatures, and estimated counting is similar to Oracle for all radionuclides and both sphere materials. At low statistics, the counting result is still good compared to Oracle. Regarding the case of the lead sphere, the estimated counting of ^{133}Ba and ^{57}Co is slightly less accurate, as the shape of their spectral signatures is more sensitive to lead thickness due to the fluorescence effect.
This study demonstrates the capabilities of the hybrid unmixing approach to handle the spectral deformations and Poisson statistics for automatic full-spectrum analysis of γ-spectra. The validation was performed assuming that the radionuclides present in a radioactive source are known. The next step is to extend this development to the identification of the radionuclides when their presence is unknown. To this end, future investigations will focus on using the model selection using a radionuclide dictionary as studied in [6][7].

Appendix A. IAE hyperparameters and implementation

Hyperparameters	Co60	Ba133	Co57	Cs137	Joint
Maximum channel	800	250	100	400	800
Solver	Adam	Adam	Adam	Adam	Adam
Learning rate	0.001	0.001	0.001	0.001	0.001
Batch size	36	36	36	36	36
Number of epochs	20000	20000	20000	20000	20000
Regulisation paramater	0.001	0.001	0.001	0.001	0.001
Encoder: numbers of layers	6	6	6	6	6
Activation	Elu(alpha=1)	Elu(alpha=1)	Elu(alpha=1)	Elu(alpha=1)	Elu(alpha=1)
Encoder 1 : Conv1D (in_channels, out_channels, kernel_size, stride)	1, 12, 4, 1	1, 12, 4, 1	1, 12, 4, 1	1, 12, 4, 1	4, 12, 4, 1
Encoder 2 : Conv1D	12, 12, 4, 1	12, 12, 4, 1	12, 12, 4, 1	12, 12, 4, 1	12, 12, 4, 1
Encoder 3 : Conv1D	12, 12, 6, 2	12, 12, 6, 2	12, 12, 3, 1	12, 12, 6, 2	12, 12, 6, 2
Encoder 4 : Conv1D	12, 16, 6, 2	12, 16, 6, 2	12, 16, 3, 1	12, 16, 6, 2	12, 16, 6, 2
Encoder 5 : Conv1D	16, 16, 6, 2	16, 16, 6, 2	16, 16, 3, 1	16, 16, 6, 2	16, 16, 6, 2
Encoder 6 : Conv1D	16, 16, 4, 2	16, 16, 4, 2	16, 16, 3, 1	16, 16, 4, 2	16, 16, 4, 2
cost function	log	log	log	log	mean log of each radionuclide

References

[1] S. Dragović, Artificial neural network modeling in environmental radioactivity studies–a review, Science of The Total Environment (2022) 157526.

[2] M. Kamuda, J. Stinnett, C. Sullivan, Automated isotope identification algorithm using artificial neural networks, IEEE Transactions on Nuclear Science 64 (7) (2017) 1858–1864.

[3] G. Daniel, F. Ceraudo, O. Limousin, D. Maier, A. Meuris, Automatic and real-time identification of radionuclides in gamma-ray spectra: a new method based on convolutional neural network trained with synthetic data set, IEEE Transactions on Nuclear Science 67 (4) (2020) 644–653.

[4] S. Galib, P. Bhowmik, A. Avachat, H. Lee, A comparative study of machine learning methods for automated identification of radioisotopes using nai gamma-ray spectra, Nuclear Engineering and Technology 53 (12) (2021) 4072–4079.

[5] Z. Chaouai, G. Daniel, J.-M. Martinez, O. Limousin, A. Benoit-Lévy, Application of adversarial learning for identification of radionuclides in gamma-ray spectra, Nuclear Instruments and Methods in Physics Research Section A: Accelerators, Spectrometers, Detectors and Associated Equipment 1033 (2022) 166670.

[6] R. André, C. Bobin, J. Bobin, J. Xu, A. de Vismes Ott, Metrological approach of γ-emitting radionuclides identification at low statistics: application of sparse spectral unmixing to scintillation detectors, Metrologia 58 (1) (2021) 015011.

[7] J. Xu, J. Bobin, A. de Vismes Ott, C. Bobin, Sparse spectral unmixing for activity estimation in γ-ray spectrometry applied to environmental measurements, Applied Radiation and Isotopes 156 (2020) 108903.

[8] F. M. de Oliveira, G. Daniel, O. Limousin, Artificial gamma ray spectra simulation using generative adversarial networks (gans) and supervised generative networks (sgns), Nuclear Instruments and Methods in Physics Research Section A: Accelerators, Spectrometers, Detectors and Associated Equipment 1047 (2023) 167795.

[9] A. N. Turner, C. Wheldon, T. K. Wheldon, M. R. Gilbert, L. W. Packer, J. Burns, M. Freer, Convolutional neural networks for challenges in automated nuclide identification, Sensors 21 (15) (2021) 5238.

[10] S. Agostinelli, J. Allison, K. a. Amako, J. Apostolakis, H. Araujo, P. Arce, M. Asai, D. Axen, S. Banerjee, G. Barrand, et al., Geant4a simulation toolkit, Nuclear instruments and methods in physics research section A: Accelerators, Spectrometers, Detectors and Associated Equipment 506 (3) (2003) 250–303.

[11] American national standard for performance criteria for spectroscopy-based portal monitors used in homeland security, ANSI N42.38-2015 (Revision of ANSI N42.38-2006) (2016) 1–59.

[12] J. Bobin, R. C. Gertosio, C. Bobin, C. Thiam, An autoencoder-based model for learning regularizations in unmixing problems, Digital Signal Processing (2023) 104058.

[13] A. Paszke, S. Gross, F. Massa, A. Lerer, J. Bradbury, G. Chanan, T. Killeen, Z. Lin, N. Gimelshein, L. Antiga, A. Desmaison, A. Kopf, E. Yang, Z. DeVito, M. Raison, A. Tejani, S. Chilamkurthy, B. Steiner, L. Fang, J. Bai, S. Chintala, Pytorch: An imperative style, high-performance deep learning library, in: Advances in Neural Information Processing Systems 32, Curran Associates, Inc., 2019, pp. 8024–8035.

[14] D. Kraft, A software package for sequential quadratic programming, Forschungsbericht- Deutsche Forschungs- und Versuchsanstalt fur Luft- und Raumfahrt (1988).

[15] Y. Xu, W. Yin, A globally convergent algorithm for nonconvex optimization based on block coordinate update, Journal of Scientific Computing 72 (2) (2017) 700–734.

[16] D. Lee, H. S. Seung, Algorithms for non-negative matrix factorization, Advances in neural information processing systems 13 (2000).

Declaration of interests

☒ The authors declare that they have no known competing financial interests or personal relationships that could have appeared to influence the work reported in this paper.

☐ The authors declare the following financial interests/personal relationships which may be considered as potential competing interests: